Journal of Catalysis 271 (2010) 305-314

Structure and properties of a Mo oxide catalyst supported on hollow carbon nanofibers in selective propene oxidation

T. Ressler[*1], A. Walter[1], J. Scholz [1], J.-P. Tessonnier [2], D. S. Su [2]

[1] Institut für Chemie, Technische Universität Berlin, Strasse des 17. Juni 135, 10623 Berlin, Germany
[2]Fritz-Haber-Institut der Max-Planck-Gesellschaft, Departement of Inorganic Chemistry, D-14195 Berlin, Germany

[*] Corresponding author: e-mail Thorsten.ressler@tu-berlin.de,

Received 2 November 2009; revised 2 February 2010; accepted 3 February 2010. online 16 March 2010.

Abstract

In situ X-ray absorption spectroscopy (XAS) under reaction conditions of selective propene oxidation was employed to elucidate the local structure of as-prepared and activated molybdenum oxide supported on hollow vapor-grown carbon nanofibers (VGCNF). The local structure of as-prepared Mo_xO_y-VGCNF was very similar to that of hexagonal MoO_3. During heat treatment in propene- and oxygen-containing atmosphere, as-prepared Mo_xO_y-VGCNF transforms into activated Mo_xO_y-VGCNF above 623 K. The local structure around the Mo centers in activated Mo_xO_y-VGCNF is similar to that of α-MoO_3. Temperature- and time-dependent XAS measurements showed a rapid transformation from hex-MoO_3 to α-MoO_3 supported on VGCNF under reaction conditions. Subsequently, the resulting activated Mo_xO_y-VGCNF catalyst exhibited a slowly increasing average oxidation state. The latter coincided with the formation of acrylic acid, which is hardly detectable during catalysis on regular, binary α-MoO_3. Moreover, activated Mo_xO_y-VGCNF is much more active in the selective oxidation of propene compared to α-MoO_3. The correlation between catalytic selectivity and average oxidation state as a result of suitable reduction–oxidation kinetics corroborates the importance of structural complexity rather than chemical complexity.

Keywords: Heterogeneous catalysis; Structure–activity relationships; EXAFS spectroscopy; X-ray absorption; Molybdenum; Oxides; Support; Carbon nanofibers; Selective oxidation; Propene

1. Introduction

Mixed oxide catalysts containing metals from group 5 or 6 of the Periodic Table are active in selective oxidation of propane to acrolein and acrylic acid [1-6]. Detailed studies on the correlations between structure and performance are required to reveal the role of catalyst structure and composition. The reduced chemical complexity of binary oxides makes them preferred model systems to distinguish between structural and compositional effects on catalytic performance. α-MoO_3 constitutes the room temperature stable modification with Mo(VI) centers in the highest oxidation state. Hence, α-MoO_3 would be the simplest binary model system available for studying structure–activity correlations. Detailed studies on the characteristic defect structure of α-MoO_3 under propene oxidation conditions revealed a slightly decreased average Mo valence caused by slow re-oxidation kinetics [7,8]. The latter is correlated with the formation of shear-structural defects in the layer structure of bulk α-MoO_3. However, α-MoO_3 exhibits only moderate activity in propene oxidation with rather poor selectivity toward acrolein or acrylic acid. Furthermore, other binary modifications of hexavalent molybdenum like hexagonal MoO_3 are not stable under reaction conditions above 623 K and readily decompose to α-MoO_3 [9]. Similarly, binary bulk Mo oxides with average valences between 6.0 and 4.0 (like Mo_4O_{11}, Mo_8O_{23}, etc.) are oxidized to α-MoO_3 under selective oxidation conditions.

In order to modify the structure of binary molybdenum oxides while maintaining structural stability above 673 K, supporting oxide species on various oxidic or carbonaceous supports is currently employed extensively by many researchers [10-13]. Supported binary metal oxides may exhibit particular metal oxide structures which are not

stable and, thus, not available for investigations under reaction conditions. We have shown recently that hexagonal MoO_3 supported on nanostructured SiO_2 is stable under selective oxidation conditions up to 773 K [9]. Moreover, dispersed supported metal oxides simplify correlating the local structure around the metal centers with their catalytic performance. Distinguishing active metal centers at the surface from metal centers in the bulk of conventional oxide catalysts is no longer required. Here, we have employed hollow vapor-grown carbon nanofibers (VGCNF) as support material for binary molybdenum oxide species as selective oxidation catalysts. Carbon nanotubes and nanofibers are progressively employed as catalyst support for many reactions. Compared to other supports, they are chemically stable in most aggressive media, they show a high thermal conductivity and offer the possibility to chemically modify their surface [14]. These materials also exhibit less than a monolayer of oxygen, only present at the surface. Therefore, the characterization of supported transition metal oxide catalysts with techniques such as X-ray photoelectron spectroscopy (XPS) or electron energy loss spectroscopy (EELS) is significantly easier than when oxidic supports are used. In addition, as for carbon nanotubes, VGCNFs show a smooth surface and are quasi transparent under the beam of the transmission electron microscope (TEM). The morphological (sintering) as well as the structural (phase transition) changes occurring during the catalytic reaction can be easily accessed when investigating the spent catalyst.

Obtaining structure property relationships of supported metal oxide catalysts is not a simple task. It requires experimental techniques that permit in situ studies under relevant reaction conditions at a suitable time resolution. X-ray absorption spectroscopy (XAS) is particularly suitable to study the supported catalysts under reaction conditions [9,15,16]. The electronic structure of the constituent metals in the oxide catalyst is obtained from analyzing the near-edge region of the absorption spectrum. Moreover, geometric structural parameters like coordination numbers, nearest neighbor distances, and disorder parameters may be determined by fitting suitable theoretical model structures to experimental spectra. Here, we have performed in situ XAS investigations of molybdenum oxide supported on carbon nanofibers. Our approach focused on elucidating both the local structure around the Mo centers in the as-prepared and the activated model catalysts and the structural dynamics under changing reaction conditions.

2. Experimental

2.1. Sample preparation

Open, hollow vapor-grown carbon nanofibers (VGCNFs) were purchased from Pyrograf Products Inc., USA (Pyrograf-III, product PR24-PS). A detailed characterization of the pristine nanofibers is provided elsewhere [17]. Briefly, the VGCNFs exhibit average internal and external diameters of 40 and 90 nm, respectively, and lengths up to few hundred micrometers. The specific surface area of the VGCNFs was 43 m^2/g. The pristine nanofibers were functionalized with concentrated nitric acid (65%) at 373 K for 16 h before use. Deposition of the molybdenum oxide was done by the incipient wetness impregnation technique using a solution of ammonium heptamolybdate ($(NH_4)_6Mo_7O_{24}\cdot 4H_2O$, Fluka) with the acidity adjusted to pH 3 with nitric acid. The concentration of the solution was set so the final metal loading of 7 wt.% Mo (10 wt.% on a MoO_3 basis). After deposition, the sample was dried at room temperature for 10 h and at 373 K for 5 h and subsequently calcined at 623 K for 2 h. The resulting material is denoted as Mo_xO_y-VGCNF, material treated at temperatures above 623 K is denoted as activated Mo_xO_y-VGCNF. Sample preparation and characterization have been described in detail in Ref. [18]. Electron microscopy studies revealed a disordered Mo_xO_y layer on the surface of the VGCNF with a thickness of about 1 nm. Distinct Mo oxide phase or particles of molybdenum oxides were detected neither in the as-prepared nor in the spent Mo_xO_y-VGCNF catalyst. Additionally, no crystalline Mo oxide phases were detected in the as-prepared and spent Mo_xO_y-VGCNF materials by X-ray diffraction. This corroborated a crystallite size of Mo oxide species of less than 2–4 nm. Moreover, no bulk α-MoO_3 or other molybdenum oxides were detectable by Raman spectroscopy in the as-prepared Mo_xO_y-VGCNF material.

2.2. X-ray absorption spectroscopy (XAS)

In situ transmission XAS experiments were performed at the Mo K edge (20.0 keV) at beamline X1 at the Hamburg Synchrotron Radiation Laboratory, HASYLAB, using a Si(311) double-crystal monochromator. EXAFS spectra at the Mo K edge in the k space up to 14 $Å^{-1}$ were measured in ≈4 min. For a better time resolution during isothermal experiments at elevated temperatures, Mo K XANES spectra (19.9–20.3 keV) were measured in ≈30 s. For in situ XAFS and catalysis measurements, 23 mg of Mo_xO_y-VGCNF were pressed into self-supporting pellets (5 mm in diameter) resulting in an edge jump, $\Delta\mu_x$, at the Mo K of about 0.6. Measurements of α-MoO_3 and hex-MoO_3 references have been previously described [9]. Transmission XAS measurements were performed in a suitable in situ cell [19]. Temperature-programmed reduction was conducted in 3% propene and He (total flow 30 ml/min) in a temperature range from 293 K to 773 K at a heating rate of 5 K/min. Reaction tests were performed in 10% propene/10% O_2 in He or 3% propene/10% O_2 in He in the temperature range from 293 K to 723 K or 293 K to 673 K, respectively (5 K/min, total flow 30 ml/min). The gas atmosphere was analyzed using a noncalibrated mass

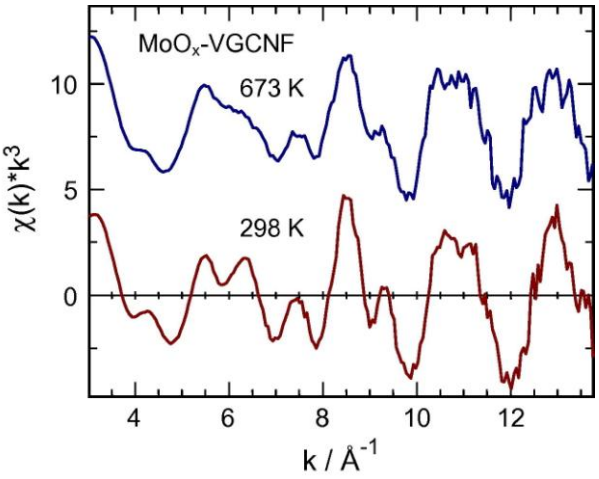

Fig. 1: Mo K edge XAFS $\chi(k) * k^3$ of as-prepared and thermally treated Mo_xO_y-VGCNF at 298 K and 673 K, respectively.

spectrometer in a multiple ion detection mode (QMS200 from Pfeiffer).

X-ray absorption fine structure (XAFS) analysis was performed using the software package WinXAS v3.2 [20]. Background subtraction and normalization were carried out by fitting linear polynomials to the pre-edge and 3rd degree polynomials to the post-edge region of an absorption spectrum, respectively. The extended X-ray absorption fine structure (EXAFS) $\chi(k)$ was extracted by using cubic splines to obtain a smooth atomic background $\mu_0(k)$. The FT($\chi(k) * k^3$), often referred to as pseudo radial distribution function, was calculated by Fourier transforming the k^3-weighted experimental $\chi(k)$ function, multiplied by a Bessel window, into the R space. EXAFS data analysis was performed using theoretical backscattering phases and amplitudes calculated with the ab-initio multiple-scattering code FEFF7 [21]. EXAFS refinements were performed in R space simultaneously to magnitude and imaginary part of a Fourier transformed k^3-weighted and k^1-weighted experimental $\chi(k)$ using the standard EXAFS formula [22]. This procedure strongly reduces the correlation between the various XAFS fitting parameters. Structural parameters allowed to vary in the refinement were (i) disorder parameter σ^2 of selected single-scattering paths assuming a symmetrical pair-distribution function and (ii) distances of selected single-scattering paths. Coordination numbers (CN), E_0 shifts, and amplitude reduction factor S_0^2 were kept invariant in the final fitting procedures. Correlations of specific parameters to reduce the number of free running parameters and to improve the stability of the refinement are described below.

The statistical significance of the fitting procedure employed was carefully evaluated in three steps [15]. The procedures used largely correspond to recommendations of the *International X-ray Absorption Society* on criteria and error reports [23]. First, the number of independent parameters (N_{ind}) was calculated according to the Nyquist theorem $N_{ind} = 2/\pi * \Delta R * \Delta k + 2$. In all cases the number of free running parameters in the refinements was well below N_{ind}. Second, confidence limits were calculated for each individual parameter. In the corresponding procedure, one parameter was successively varied by a certain percentage (i.e. 0.05% for R and 5% for σ^2) and the refinement was restarted with this parameter kept invariant. The parameter was repeatedly increased or decreased until the fit residual exceed the original fit residual by more than 5%. Eventually, the confidence limit of the parameter was obtained from linear interpolation between the last and second last increment for an increase in fit residual of 5%. This procedure was consecutively performed for each fitting parameter. Third, a so-called F test was performed to assess the significance of the effect of additional fitting parameters on the fit residual [24]. Fit parameters employed exhibited F values below 0.2 and are statistically significant.

2.3. Quantitative catalysis measurements

Quantitative catalysis measurements were performed in the laboratory using the XAS in situ cell connected to an online gas chromatography system (Varian CP-3800) and a noncalibrated mass spectrometer (Pfeiffer QMS). Hydrocarbons and oxygenated reaction products were analyzed using a Carbowax 52CB capillary column connected to a Al_2O_3/MAPD capillary column or a fused silica restriction (25 m × 0.32 mm) each connected to a flame ionization detector (FID). Reactant gas flow rates of oxygen, propene, and Helium were adjusted through separate mass flow controllers to a total flow of 40 ml/min. A mixture of 5% propene and 5% oxygen in helium was used for catalytic tests in the range of 295–748 K. Sample mass, BN diluent, and pellet preparation were the same as for the XAFS studies.

3. Results and discussion

3.1. Local structure of as-prepared Mo oxide species on VGCNF

The EXAFS $\chi(k)$ of as-prepared and thermally treated Mo_xO_y-VGCNF are depicted in Fig. 1. Apparently, the data quality obtained permits reliable data analysis up to ~14 $Å^{-1}$ even under reaction conditions at temperatures above 623 K. The XANES spectrum of Mo_xO_y-VGCNF is shown together with those of hexagonal MoO_3 and α-MoO_3 in Fig. 2. The structural relationship between these two modifications will be discussed below. Comparison with the spectra of those references indicates a local structure around the Mo centers in Mo_xO_y-VGCNF related to that in bulk molybdenum trioxides. Magnitude and imaginary part of the FT($\chi(k) * k^3$) of Mo_xO_y-VGCNF are compared to that of hex-MoO_3 and α-MoO_3 in Fig. 3. Shape and peak positions of the FT($\chi(k) * k^3$) of Mo_xO_y-VGCNF appear to be more similar to that of the hexagonal modification of MoO_3 (Fig. 3a). A good agreement in the ranges from 1 to 2 Å and 4 to 6 Å can be seen. Between 2 and 4 Å, the amplitude

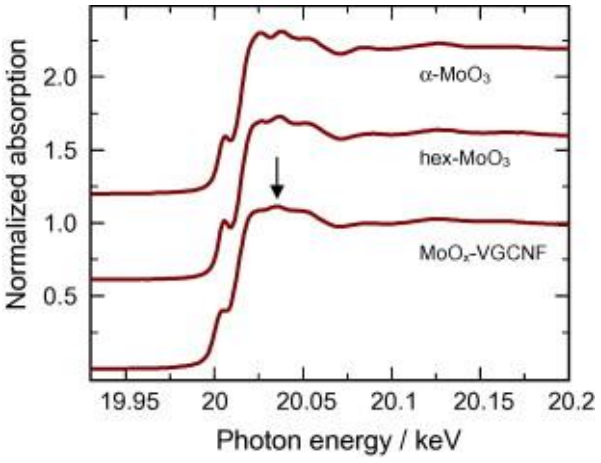

Fig. 2: Mo K edge XANES spectra of Mo_xO_y-VGCNF compared to the spectra of references α-MoO_3 and hex-MoO_3 (arrow indicates features used for calculating average valence).

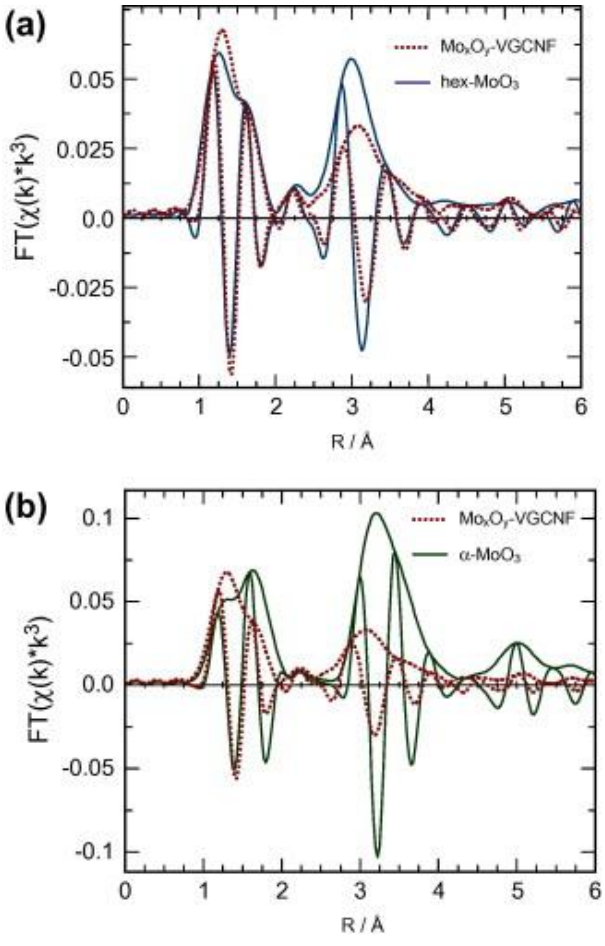

Fig. 3: Magnitude and imaginary part of FT($\chi(k) * k^3$) of Mo_xO_y-VGCNF compared to that of reference hex-MoO_3 (a) and α-MoO_3 (b).

of Mo_xO_y-VGCNF is reduced compared to hex-MoO_3. Apparently, hex-MoO_3 is a suitable model system to simulate the experimental spectra of Mo_xO_y-VGCNF. Hence, a theoretical XAFS function calculated for a hex-MoO_3 model structure was refined to the FT($\chi(k) * k^3$) of as-prepared Mo_xO_y-VGCNF. Additionally, the same procedure was applied to simulate the FT($\chi(k) * k^3$) of crystalline bulk references hex-MoO_3 and α-MoO_3. The resulting theoretical and experimental FT($\chi(k) * k^3$) as-prepared Mo_xO_y-VGCNF are depicted in Fig. 4. The corresponding fitting parameters are given in Table 1.

The fitting procedure chosen was equally well suited to simulate the experimental FT($\chi(k) * k^3$) of both as-prepared Mo_xO_y-VGCNF and references hex-MoO_3 and α-MoO_3 (Table 1). The good agreement between theoretical and experimental FT($\chi(k) * k^3$) of Mo_xO_y-VGCNF (Fig. 4) confirmed that the local structure of the Mo oxide species supported on VGCNF can be well described by that of hexagonal MoO_3. Characteristic Mo–O and Mo–Mo paths in the local structure of hex-MoO_3 and the corresponding single-scattering FT($\chi(k) * k^3$) are also shown in Fig. 4. The Mo–Mo distances required to describe the experimental FT($\chi(k) * k^3$) of Mo_xO_y-VGCNF and the reference materials include one in-plane distance of corner-sharing MoO_6 units and two distances of corner-sharing and edge-sharing MoO_6 units perpendicular to the basal plane of hex-MoO_3. This structural arrangement indicates a three-dimensional MoO_3 structure supported on VGCNF. Given the k range used for EXAFS refinement, the spatial resolution according to $dR = \pi/2k_{max}$ with $k_{max} = 14$ Å^{-1} amounted to $dR = 0.11$ Å. Therefore, and in addition to the results of the statistical evaluation, distances and σ^2 parameters of the first two Mo–O pairs (i.e. 1.69 Å and 1.75 Å; 1.97 Å and 2.21 Å) were refined the same (i.e. the corresponding differences ΔR with respect to the hex-MoO_3 model structure were refined the same).

The reference hex-MoO_3 measured corresponds to a mechanical mixture of bulk hex-MoO_3 and VGCNF in a similar ratio as the Mo_xO_y-VGCNF material (Fig. 2). The XANES and EXAFS spectra of this reference are similar to those of bulk hex-MoO_3. Conversely, the amplitude of the XANES features of Mo_xO_y-VGCNF appeared to be reduced compared to the reference oxides. Moreover, the FT($\chi(k) * k^3$) of Mo_xO_y-VGCNF also exhibited a slightly reduced amplitude for the higher Mo–Mo shells (Fig. 3). This reduced amplitude may be caused by the small size of the oxide particles (reduced average CN) or static disorder in the particles (broadened distance distribution increases σ^2). In principal, XAFS data analysis should be able to distinguish both effects by simultaneously refining CN and σ^2 in the corresponding fitting procedure. However, evaluating the correlation between these parameters revealed that this was not feasible. Fitting results of an EXAFS refinement procedure using free coordination numbers and σ^2 parameters to simulate the experimental FT($\chi(k) * k^3$) of reference hexagonal MoO_3 are given in Table 2. While Mo–O and Mo–Mo distances are in good agreement with the crystallographic structure of hex-MoO_3 (Table 1), coordination numbers CN considerably exceed the crystallographic values. The corresponding σ^2 parameters are also increased compared to the parameters given in Table 1 to account for the increased amplitude. Moreover, calculations

Table 1: Type and number (N) of atoms at distance R from the absorbing Mo atom in the local structure of α-MoO_3, hex-MoO_3, and as-prepared Mo_xO_y-VGCNF. Experimental distances and XAFS disorder parameters (σ^2) were obtained from the refinement of a hex-MoO_3 model structure to the experimental Mo K edge XAFS FT($\chi(k) * k^3$) of α-MoO_3 (residual 9.0), hex-MoO_3 (residual 9.7), and as-prepared Mo_xO_y-VGCNF (residual 7.8) (Fig. 4) (k range from 3.0 to 14.0 Å^{-1}, R range 0.9–4.0 Å, N_{ind} = 24, E_0 = 0 eV, N_{free} = 11). Subscript C indicates parameters that were correlated in the refinement (same ΔR with respect to model structure or σ^2). Confidence limits of refined parameters are included.

Type	N	α-MoO_3			Hex-MoO_3			As-prep Mo_xO_y-VGCNF	
		R_T (Å)	R_E (Å)	σ^2 (Å^2)	R_T (Å)	R_E (Å)	σ^2 (Å^2)	R (Å)	σ^2 (Å^2)
Mo–O	1	1.67	1.69	0.0025	1.68	1.69	0.0014	1.69 ± 0.008	0.0008 ± 0.0001
Mo–O	1	1.73	1.75$_C$	0.0025$_C$	1.73	1.75$_C$	0.0014$_C$	1.75$_C$	0.0008$_C$
Mo–O	2	1.95	1.97	0.0012	1.97	1.97	0.0036	1.97 ± 0.006	0.0041 ± 0.0003
Mo–O	1	2.25	2.21$_C$	0.0012$_C$	2.21	2.21$_C$	0.0036$_C$	2.21$_C$	0.0041$_C$
Mo–O	1	2.33	2.35	0.0017	2.39	2.39	0.0016	2.40 ± 0.008	0.0028 ± 0.001
Mo–Mo	2	3.44	3.44	0.0025	3.31	3.36	0.0035	3.37 ± 0.004	0.0068 ± 0.0003
Mo–Mo	2	3.70	3.75	0.0025$_C$	3.73	3.76	0.0035$_C$	3.79 ± 0.007	0.0068$_C$
Mo–Mo	2	3.97	4.07	0.004	4.03	3.95	0.0089	4.03 ± 0.01	0.0109 ± 0.003

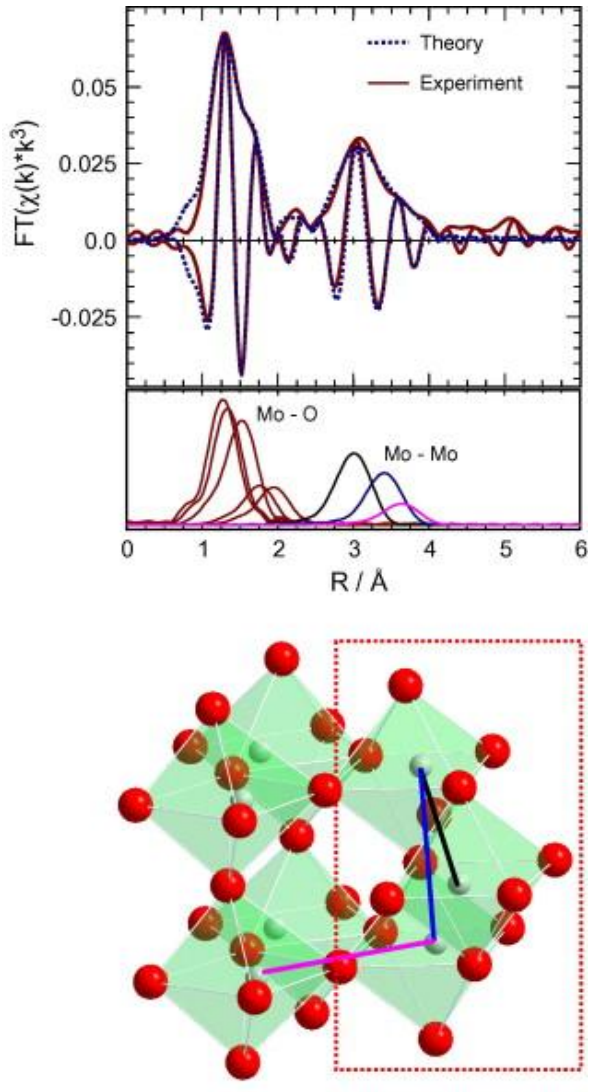

Fig. 4: Experimental (solid) Mo K edge FT($\chi(k) * k^3$) of Mo_xO_y-VGCNF together with a theoretical XAFS function (fitting results are given in Table 1). FT($\chi(k) * k^3$) of the individual Mo–O and Mo–Mo scattering paths and a schematic representation of the local structure of hex-MoO_3 (dotted rectangle emphasizes building unit of hex-MoO_3 and α-MoO_3).

of confidence intervals resulted in very large values for the Mo–Mo coordination numbers. Hence, in particular, CN and σ^2 parameters were strongly correlated, and corresponding fitting procedures with independent CN and σ^2 resulted in very large uncertainties.

Apparently, EXAFS fitting procedures with independent CN and σ^2 are not even suited to simulate the FT($\chi(k) * k^3$) of an ideal reference MoO_3. Thus, two approaches were attempted to keep either CN or σ^2 invariant in the refinements. First, varying CN and fixing σ^2 to values determined for crystalline bulk references and, second, fixing CN to bulk values and varying σ^2. It was found that the second approach yielded the lowest fit residual (7.8) compared to the first approach (9.9). Hence, we decided to account for the reduced amplitude by refining only the disorder parameter σ^2. A physical interpretation of σ^2 in terms of particle sizes, however, is hardly possible. Eventually, we may speculate that static disorder in the supported Mo oxide phase contributed more to the reduced amplitude of the FT($\chi(k) * k^3$) of Mo_xO_y-VGCNF than the average coordination number in the small particles. In conclusion, we suggest that the reduced FT amplitudes correspond to small disordered particles or reduced extension of the hexagonal MoO_3 structure on the VGCNF support. This agrees with previous electron microscopy and Raman studies which showed no detectable amount of bulk MoO_3 phases. Apparently, the carbon nanofibers support a dispersed molybdenum oxide species with a local structure similar to that of hex-MoO_3.

α-MoO_3 and hexagonal MoO_3 exhibit a distinct structural relationship that is readily visible in the very similar XANES spectra, FT($\chi(k) * k^3$), and structural parameters given in Table 1. A similar spectroscopic fingerprint of the two references is caused by the same building block consisting of three edge and corner-sharing MoO_6 units (Fig. 4). The structural relationship is also visible in the schematic representation of α-MoO_3 and hexagonal MoO_3 depicted in Fig. 5. The similarity between the two structures suggests an easy and rapid transformation from hexagonal MoO_3 to orthorhombic α-MoO_3. Mo–O and Mo–Mo distances around the Mo absorber in α-MoO_3 and hex-MoO_3 are given in Table 1. Despite their different long-range order structures, the local structure around the Mo

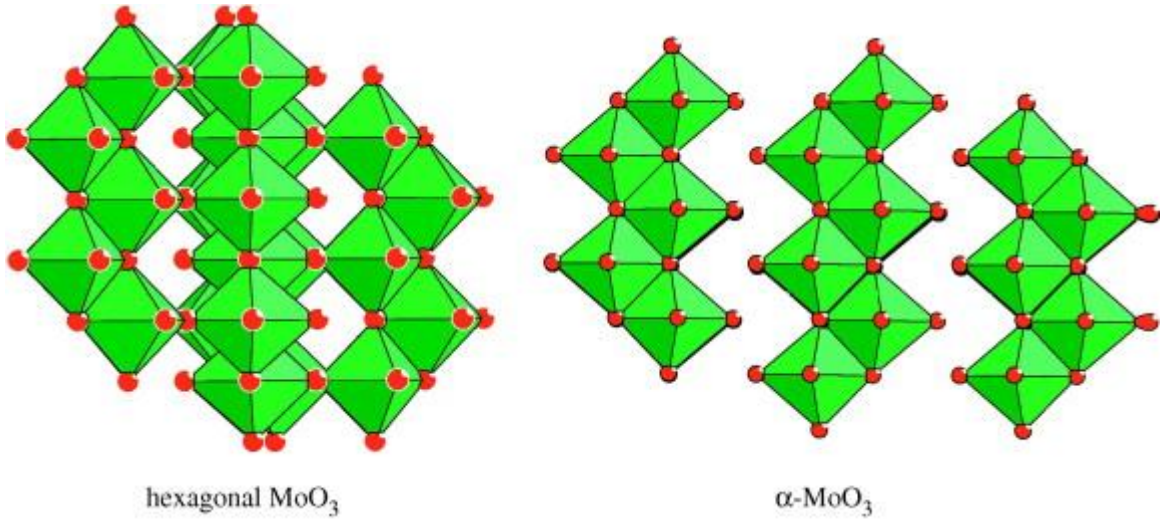

Fig. 5: Schematic representation of the structure of hex-MoO_3 and α-MoO_3. The orientation was chosen to emphasize the structural relationship.

Table 2: Type and number (N) of atoms at distance R from the absorbing Mo atom in the local structure of hex-MoO_3. Experimental coordination numbers, distances, and XAFS disorder parameters (σ^2) were obtained from the refinement of a hex-MoO_3 model structure to the experimental Mo K edge XAFS FT($\chi(k)$ * k^3) of hex-MoO_3 (k range from 3.0 to 14.0 Å^{-1}, R range 0.9–4.0 Å, N_{ind} = 24, E_0 = 0 eV, fit residual 8.5, N_{free} = 14). Subscript C indicates parameters that were correlated in the refinement (same ΔR with respect to model structure or σ^2). Confidence limits of refined parameters are included.

Type	Model hex-MoO_3		Experimental reference hex-MoO_3		
	N	R (Å)	N	R	σ^2
Mo–O	1	1.68	1	1.69 ± 0.002	0.0012 ± 0.0002
Mo–O	1	1.73	1	1.75_C	0.0012_C
Mo–O	2	1.97	2	1.97 ± 0.005	0.0036 ± 0.0004
Mo–O	1	2.21	1	2.21_C	0.0036_C
Mo–O	1	2.39	1	2.39 ± 0.02	0.0031 ± 0.002
Mo–Mo	2	3.31	4.6 ± 3.8	3.37 ± 0.007	0.0084 ± 0.0002
Mo–Mo	2	3.73	3.2 ± 1.9	3.81 ± 0.008	0.0084_C
Mo–Mo	2	4.03	2.5 ± 3.0	4.02 ± 0.05	0.0081 ± 0.001

centers in α-MoO_3 and hex-MoO_3 is very similar. While the building blocks of α-MoO_3 and hex-MoO_3 possess the same coordination numbers, minor deviations exist in characteristic Mo–O distances (e.g. 2.35 Å [α-MoO_3] and 2.39 Å [hex-MoO_3]) and Mo–Mo distances (e.g. 3.44 and 4.07 Å [α-MoO_3] and 3.36 and 3.95 Å [hex-MoO_3]). With respect to the corresponding confidence limits given in Table 1, it appears that the fitting procedure employed permits distinguishing the local structure of α-MoO_3 and hex-MoO_3.

During decomposition of ammonium heptamolybdate, hex-MoO_3 is formed as an intermediate which rapidly transforms into α-MoO_3 at temperatures above 623 K [25]. The latter is accompanied by the evolution of ammonia or water from the channels of hex-MoO_3. Sufficiently strong support–metal oxide interaction can stabilize the channel structure of hex-MoO_3 even at temperatures up to 773 K and prevent transformation to α-MoO_3. This was recently shown for hex-MoO_3 supported on SiO_2 (SBA-15) [9]. The Mo_xO_y-VGCNF sample was calcined at 623 K, which may explain the presence of hex-MoO_3 as major phase supported on VGCNF. The strength of the interaction between Mo oxide and VGCNF in Mo_xO_y-VGCNF was further investigated by temperature-programmed reduction and reaction in propene and propene/oxygen, respectively.

3.2. Reactivity of as-prepared Mo oxide species on VGCNF

Evolution of Mo K edge XANES spectra of Mo_xO_y-VGCNF during temperature-programmed reduction in 3% propene in the temperature range from 300 K to 773 K is depicted in Fig. 6. A characteristic change in the near-edge structure can be seen at ≃623 K that corresponds to the reduction of MoO_3 to MoO_2. Similar to bulk hex-MoO_3 or α-MoO_3, Mo_xO_y-VGCNF is readily reduced in a propene atmosphere at elevated temperatures. This is in contrast to hex-MoO_3 stabilized on SBA-15, which showed no deep reduction and formation of MoO_2 even at 773 K in propene [9]. Compared to SBA-15, the metal oxide–support interaction in Mo_xO_y-VGCNF appears to be weaker and not sufficient to stabilize hex-MoO_3 at high temperatures.

Temperature-programmed reaction studies were first conducted in 10% propene and 10% oxygen in He. Evolution of Mo K edge XANES spectra and FT($\chi(k)$ * k^3) of Mo_xO_y-VGCNF in the temperature range from 300 K to 723 K is depicted in Fig. 7. Interestingly, Mo_xO_y-VGCNF exhibited a reduction to MoO_2 at ≃723 K. Upon cooling to 623 K in propene and oxygen, the material was re-oxidized to α-MoO_3. Neither α-MoO_3 nor bulk hex-MoO_3 showed a similar intermediate reduction in our previous investigations. Apparently, interaction with the VGCNF results in a highly reactive MoO_3, which despite the presence of oxygen in the gas phase is temporarily reduced in an equal

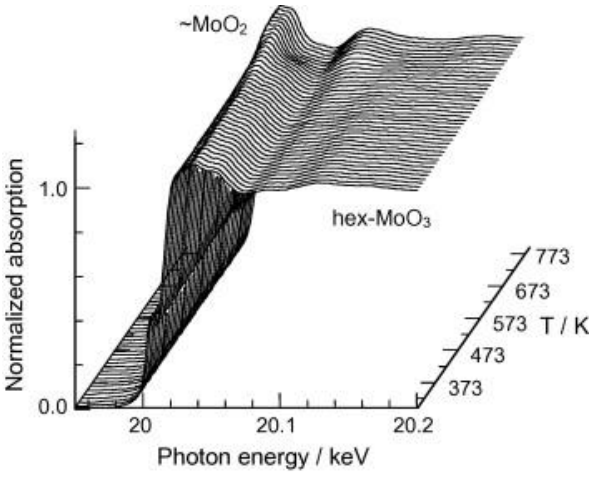

Fig. 6: Evolution of Mo K edge XANES spectra of Mo_xO_y-VGCNF measured during temperature-programmed reduction in 3% propene in He (298–773 K, 4 K/min, major MoO_x species on VGCNF are indicated).

mixture of propene and oxygen. In order to avoid reduction of Mo_xO_y-VGCNF in propene/oxygen, the concentration of propene in the gas phase and the reaction temperature were lowered. Subsequent reaction experiments were performed in 3% propene and 10% oxygen at temperatures up to 673 K.

Evolution of Mo K edge XANES spectra and FT($\chi(k) * k^3$) of Mo_xO_y-VGCNF during thermal treatment in 3% propene and 10% oxygen in the temperature range from 300 K to 673 K is depicted in Fig. 8. Here, no intermediate reduction and formation of MoO_2 are observed in the XANES and EXAFS spectra. However, minor changes in the spectra can be seen at temperatures above 623 K indicative of a structural transformation of Mo_xO_y-VGCNF under reaction conditions. The FT($\chi(k) * k^3$) of activated Mo_xO_y-VGCNF is compared to that of α-MoO_3 at 673 K in Fig. 9. While differences can be observed in the amplitude of the magnitude of the FT($\chi(k) * k^3$), the imaginary part exhibits a very similar oscillatory behavior. Apparently, starting from a hexagonal MoO_3 in the as-prepared material the local structure of activated Mo_xO_y-VGCNF became more similar to that of α-MoO_3 during thermal treatment.

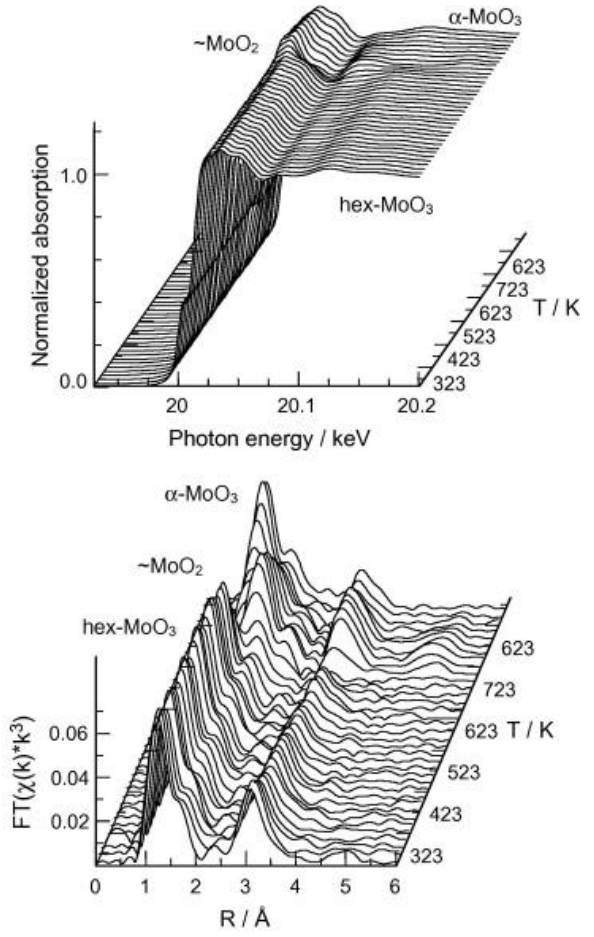

Fig. 7: Evolution of Mo K edge XANES spectra and FT($\chi(k) * k^3$) of Mo_xO_y-VGCNF measured during thermal treatment in 3% propene/10% oxygen in He (298–673 K, 5 K/min, hold at 673 K, major MoO_x species on VGCNF are indicated).

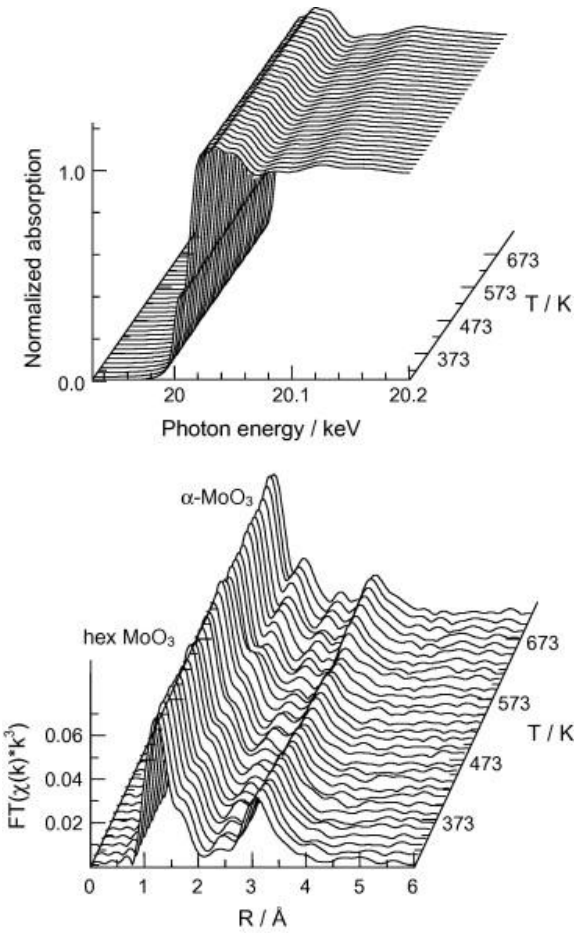

Fig. 8: Evolution of Mo K edge XANES spectra and FT($\chi(k) * k^3$) of Mo_xO_y-VGCNF measured during thermal treatment in 3% propene/10% oxygen in He (298–673 K, 5 K/min, hold at 673 K, major MoO_x species on VGCNF are indicated).

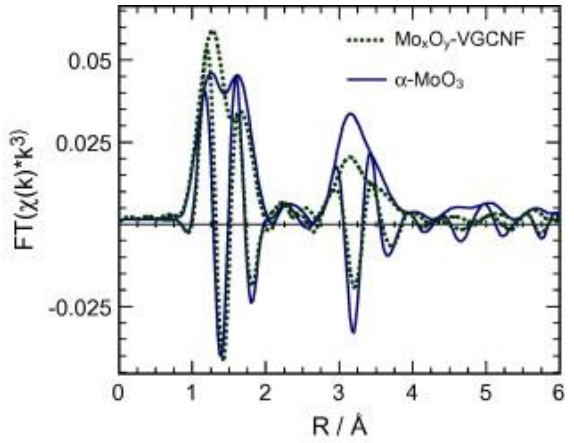

Fig. 9: Comparison of Mo K edge FT($\chi(k) * k^3$) of "activated" Mo_xO_y-VGCNF (dashed) (Fig. 8) and α-MoO_3 (solid) at 673 K.

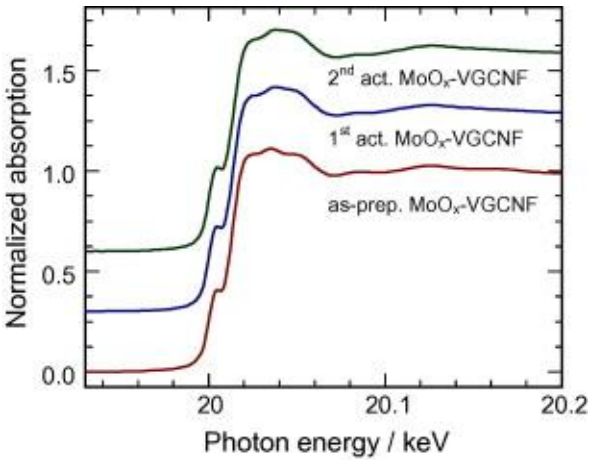

Fig. 10: Mo K edge XANES spectra of as-prepared and activated Mo_xO_y-VGCNF. Both "activated" samples were measured in 3% propene/10% oxygen at 673 K. "2nd act" corresponds to a Mo_xO_y-VGCNF sample that was previously further reduced by treatment in 3% propene at 723 K.

Somewhat in contrast to the similar FT($\chi(k) * k^3$) of α-MoO_3 and activated Mo_xO_y-VGCNF (Fig. 9), a significantly different shape of the XANES spectrum of activated Mo_xO_y-VGCNF compared to as-prepared Mo_xO_y-VGCNF (Fig. 2) and α-MoO_3 was observed (Fig. 10). This indicates a different medium-range order and electronic structure of activated Mo_xO_y-VGCNF compared to α-MoO_3 and hex-MoO_3. Moreover, reduction (723 K in 3% propene) and re-oxidation (673 K in 3% propene and 10% oxygen) of activated Mo_xO_y-VGCNF resulted in the formation of the same characteristic XANES spectrum. Apparently, the characteristic local structure of activated Mo_xO_y-VGCNF exhibited a reversible reduction and re-oxidation behavior and a pronounced stability.

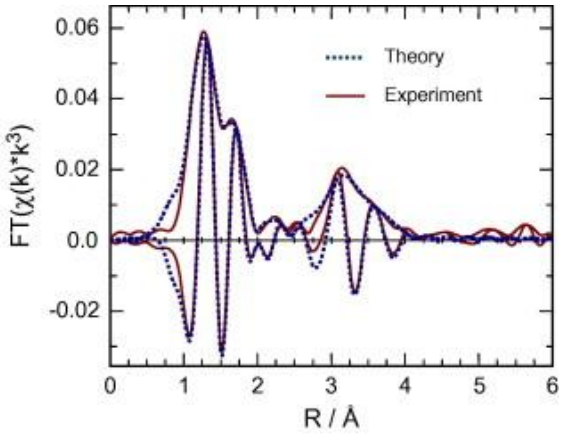

Fig. 11: Experimental (solid) Mo K edge FT($\chi(k) * k^3$) of Mo_xO_y-VGCNF measured in situ during thermal treatment in 3% propene/10% oxygen at 673 K together with a theoretical XAFS function (fitting results are given in Table 3).

3.3. Local structure of activated MoxOy-VGCNF

In order to elucidate the local structure of Mo_xO_y-VGCNF at temperatures above 623 K in propene and oxygen (i.e. activated Mo_xO_y-VGCNF), a detailed EXAFS analysis was performed. Again, the hexagonal MoO_3 model structure was chosen as starting point, and the same refinement procedure as described above was employed. Experimental and theoretical FT($\chi(k) * k^3$) of activated Mo_xO_y-VGCNF are shown in Fig. 11. The good agreement corroborates the fitting procedure chosen. Structural fitting parameters are given in Table 3. α-MoO_3 exhibits a strong anisotropic thermal expansion with a pronounced expansion along the c direction and perpendicular to the a, b layers. Therefore, α-MoO_3 measured at 673 K in air was used as reference to account for the corresponding changes in the local structure. A comparison of the structural fitting parameters of activated Mo_xO_y-VGCNF and α-MoO_3 measured at 673 K (Table 3) shows nearly identical Mo–O and Mo–Mo distances. Similar to the XAFS refinement of as-prepared Mo_xO_y-VGCNF, no reliable fitting procedure was obtained for simultaneously varying CN and σ^2. Hence, only σ^2 were allowed to vary in the refinement while CN were fixed to bulk values. An alternative approach with varying CN and fixing σ^2 to bulk values resulted in similar overall fit residual with larger confidence intervals. Because bulk hex-MoO_3 transforms to α-MoO_3 at temperatures above 623 K, no corresponding reference measurements can be performed. However, compared to the thermal treatment of hex-MoO_3 supported and stabilized on SBA-15 [9], it can be seen that the characteristic differences between the local structures in hex-MoO_3 and α-MoO_3 persist at elevated temperatures. Hence, we suggest that the local structure around the Mo centers in activated Mo_xO_y-VGCNF is very similar to that of α-MoO_3. The structural changes observed during thermal treatment of Mo_xO_y-VGCNF under reaction conditions corresponded to a transformation from hexagonal MoO_3 to α-MoO_3 (Fig. 8).

Table 3: Type and number (N) of atoms at distance R from the absorbing Mo atom in the local structure of as-prepared Mo_xO_y-VGCNF (Fig. 4), activated Mo_xO_y-VGCNF at 673 K (Fig. 11), and α-MoO_3 measured at 673 K. Experimental distances and XAFS disorder parameters (σ^2) were obtained from the refinement of a hex-MoO_3 model structure to the experimental Mo K edge XAFS FT($\chi(k) * k^3$) (k range from 3.0 to 14.0 $Å^{-1}$, R range 0.9–4.0 Å, N_{ind} = 24, E_0 = 0 eV, fit residual 8.4 for activated Mo_xO_y-VGCNF, N_{free} = 11). Subscript C indicates parameters that were correlated in the refinement (same ΔR with respect to model structure or σ^2). Confidence limits correspond to those given in Table 1.

Type	N	As-prep Mo_xO_y-VGCNF		Act Mo_xO_y-VGCNF (673 K)		α-MoO_3 (673 K)	
		R (Å)	σ^2 ($Å^2$)	R (Å)	σ^2 ($Å^2$)	R (Å)	σ^2 ($Å^2$)
Mo–O	1	1.69	0.00081	1.70	0.0012	1.69	0.0031
Mo–O	1	1.75_C	0.00081_C	1.75_C	0.0012_C	1.75_C	0.0031_C
Mo–O	2	1.97	0.0041	1.97	0.0040	1.97	0.0023
Mo–O	1	2.21_C	0.0041_C	2.20_C	0.0040_C	2.21_C	0.0023_C
Mo–O	1	2.40	0.0028	2.37	0.0029	2.38	0.0021
Mo–Mo	2	3.37	0.0068	3.42	0.0115	3.43	0.0083
Mo–Mo	2	3.79	0.0068_C	3.75	0.0115_C	3.73	0.0083_C
Mo–Mo	2	4.03	0.0109	4.08	0.0147	4.10	0.0139

3.4. Catalytic performance of activated MoxOy-VGCNF

During in situ XAS measurements of temperature-programmed treatment of Mo_xO_y-VGCNF in 3% propene and 10% oxygen (Fig. 8), the gas phase composition was continuously monitored by mass spectrometry. Evolution of normalized ion currents of selected masses (m/e) is depicted in Fig. 12. Onset of catalytic activity is observed at 573 K. Formation of total oxidation product CO_2 (m/e 44) and selective oxidation product acrolein (m/e 56) at this temperature is typical for molybdenum oxide-based catalyst. At 673 K, the formation of CO_2 strongly declined accompanied by formation of acrylic acid (m/e 72). This behavior is atypical because MoO_3 catalysts are commonly believed to be inactive for the oxidation of propene to acrylic acid.Additionally, quantitative catalytic measurements were performed at 673 K in 5% propene and 5% oxygen in helium. This reactant ratio was chosen because of specific concentration and mass flow constrains of the GC systems used. The XAS in situ cell was used as reactor. Catalyst and diluent mass were chosen according to the in situ measurements described above. Regular α-MoO_3 obtained from thermal decomposition of AHM [8] served as reference compound. The mass of α-MoO_3 was adjusted to yield a comparable Mo K edge jump for both catalysts. Conversion of propene on Mo_xO_y-VGCNF under these conditions amounted to 9% compared to 1.4% on reference α-MoO_3. Concentrations of major oxidation products measured in the in situ cell exhaust amounted to 7500 ppm and 700 ppm CO_2, 920 ppm and 110 ppm acrolein, and 120 ppm and ~1 ppm acrylic acid for Mo_xO_y-VGCNF and α-MoO_3, respectively. The catalysis data measured confirm that in situ XAS experiments were performed in the desired differential conversion regime. Furthermore, it can be noticed that the Mo_xO_y-VGCNF catalyst is much more active per Mo mass than the α-MoO_3 catalyst. It is also much more active in the selective oxidation of propene to acrylic acid.

3.5. Correlations between structure and catalytic performance of activated MoxOy-VGCNF

Structural transformation of as-prepared hexagonal Mo_xO_y-VGCNF to activated Mo_xO_y-VGCNF (Fig. 8) resembled the structural evolution of bulk hex-MoO_3 under reaction conditions [9]. However, it appears that the resulting MoO_3–CNF catalyst possessed a distinctly different catalytic behavior. The catalytic performance of α-MoO_3 obtained from bulk hex-MoO_3 is similar to that of reference α-MoO_3 prepared by thermal decomposition of ammonium heptamolybdate. The resulting α-MoO_3 is slightly active in selective oxidation of propene to acrolein. The major product, however, is carbon dioxide from total oxidation while no formation of acrylic acid is detected. Conversely, activated Mo_xO_y-VGCNF is more selective in the oxidation of propene. Interestingly, it is also more active in selective oxidation of propene to acrylic acid.

Further structure–activity correlations were derived from the in situ EXAFS data shown in Fig. 8. Evolution of the average Mo valence of Mo_xO_y-VGCNF during treatment under reaction conditions is depicted in Fig. 12. The average Mo valence was determined from a comparison to reference compounds as described in Ref. In contrast to bulk α-MoO_3 [8], Mo_xO_y-VGCNF exhibited an increasing average valence at temperatures above 623 K that coincides with the onset of catalytic activity. Eventually, the Mo centers in the Mo_xO_y-VGCNF catalyst are fully oxidized to an average valence of six. Moreover, the increase in average Mo valence is accompanied by an improved selectivity. During hold at 673 K, evolution of CO_2 strongly declines while formation of acrylic acid is detected.

Evolution of the local structure around the Mo centers in Mo_xO_y-VGCNF during treatment under reaction conditions (Fig. 8) is depicted in Fig. 13 together with evolution of normalized ion currents of acrolein (m/e 56) and acrylic acid (m/e 72). The rapid structural transformation of hex-MoO_3 to α-MoO_3 supported on VGCNF is readily visible from the characteristic lengthening of the Mo–Mo distance at ~3.4 Å at ~600 K. This rapid transformation coincides with the onset of catalytic activity and formation

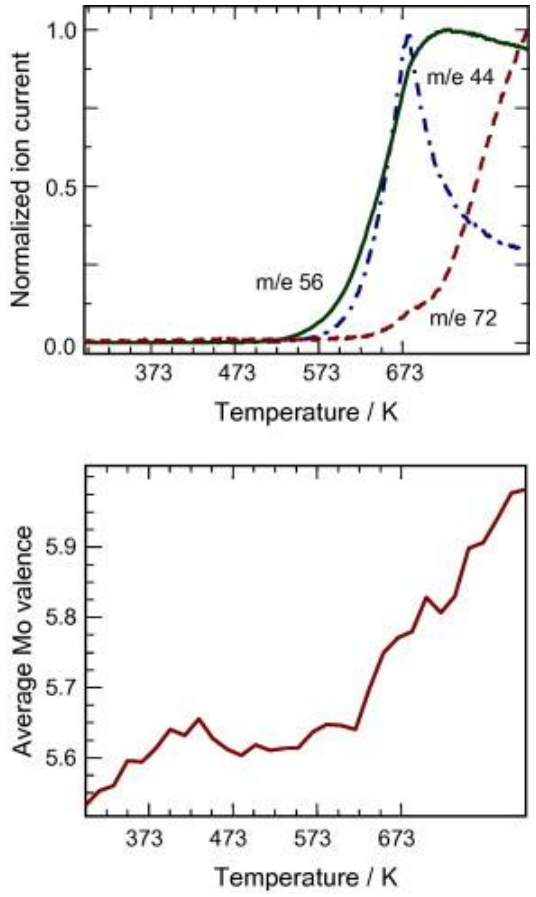

Fig. 12: (Top) evolution of normalized MS ion currents of CO_2 (m/e 44, dash-dotted), acrolein (m/e 56, solid), and acrylic acid (m/e 72, dashed) and (bottom) evolution of Mo K edge "while line" and average Mo valence during thermal treatment of Mo_xO_y-VGCNF in 3% propene/10% oxygen in He (298–673 K, 5 K/min, hold at 673 K).

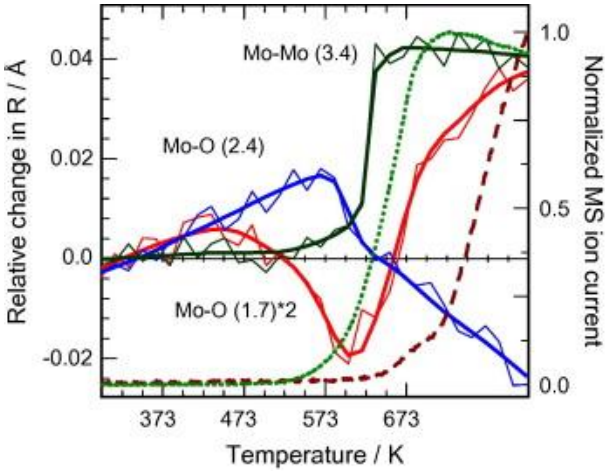

Fig. 13: Evolution of relative change in distance *R* of selected Mo–O and Mo–Mo distances in local structure of activated Mo_xO_y-VGCNF (Table 2) together with normalized MS ion current of acrolein (m/e 56, dotted) and acrylic acid (m/e 72, dashed) measured during thermal treatment of Mo_xO_y-VGCNF in 3% propene/10% oxygen in He (298–673 K, 5 K/min, hold at 673 K) (Fig. 8).

of acrolein and CO_2. Oxidation of α-MoO_3-VGCNF proceeds on a different timescale as can be seen from the slowly increasing average valence (Fig. 12) and slowly changing Mo–O distances at ∼2.4 and ∼1.7 Å.

3.6. Isothermal correlation of structure and activity of activated MoxOy-VGCNF at 673 K

In order to further elucidate and correlate structural changes and catalytic behavior, isothermal switching experiments were performed. Therefore, the gas atmosphere was rapidly switched between reducing (3% propene) and oxidizing (3% propene and 10% oxygen) conditions. Mo K edge XANES spectra were measured with a time resolution of 30 s. No EXAFS scans and, thus, no analysis of the local geometric structure were available at this measuring time. Prior to the switching experiments, the catalyst was treated in 3% propene at 723 K resulting in a slight reduction of the catalyst (average valence of ∼5.0). Evolution of Mo K edge XANES spectra of activated Mo_xO_y-VGCNF during isothermal switching experiments is shown in Fig. 14. The changes visible in the XANES region after ∼4 min correspond to the oxidation of the previously reduced Mo species to mostly MoO_3 supported on VGCNF.

The average Mo valence was again calculated from the Mo K edge position as described above. Additionally, the height of the main peak in the Mo K XANES spectrum was determined (Fig. 2). Fig. 15 shows the evolution of the MS ion currents of acrolein, CO_2, and acrylic acid during the isothermal switching experiments together with the Mo average valence and XANES peak height (Fig. 10). Changes in peak height are compared to formation of acrolein and CO_2, while changes in average valence are compared to the formation of acrylic acid. Apparently, the XANES peak height decreased very rapidly with introduction of oxygen into the reactor. This change corresponds to a rapid structural transformation of a partially reduced Mo_xO_y to MoO_3. The formation of MoO_3 supported on VGCNF coincided with the onset of catalytic activity, while the rates of acrolein and CO_2 formation, and Mo_xO_y oxidation are nearly identical.

Conversely, the average Mo valence exhibited a different time-dependent behavior. A first rapid increase in average valence after introduction of oxygen coincided with the onset of catalytic activity. Subsequently, the re-oxidation rate continuously decreased, in contrast to the XANES peak height. The shape of the valence trace resembled solid-state kinetic models with diffusion in the solid as rate-determining step. After the average Mo valence reached a value of ∼5.7, the ion currents of acrolein and CO_2 strongly decreased, accompanied by an increase in the production of acrylic acid. An average valence of six corresponding to complete re-oxidation to MoO_3 was reached after ∼1000 s. Interestingly, evolution of Mo K edge position and peak height appear to correspond to different structural changes in the activated Mo_xO_y-VGCNF catalyst.

While the edge position reflects to average Mo valence and oxidation behavior, the XANES peak height (Fig. 10) is dominated by changes in the local structure around the Mo centers in activated Mo_xO_y-VGCNF.

Structural evolution and catalytic behavior of activated Mo_xO_y-VGCNF at 673 K during switching experiments agrees well with the corresponding evolution dedepicted in [Fig. 12] and [Fig. 13]. Under both isothermal and temperature-programmed reaction conditions, formation of acrylic acid is detected. In both experiments, detection of acrylic acid was delayed with respect to the onset of catalysis and accompanied by a decrease in formation of CO_2. The latter indicates an increasing selectivity, which in both cases appears to be correlated with an increasing Mo average valence.

Both complete re-oxidation to an average Mo valence of six and formation of acrylic acid have not been observed during switching experiments with bulk α-MoO_3. Because of the characteristic defects formed in the three-dimensional layer structure of α-MoO_3 below 700 K [7] and [8], the re-oxidation rate under reaction conditions remains lower than the reduction rate. This leads to an average Mo valence lower than six for bulk α-MoO_3 under propene oxidation conditions. Accordingly, the partially reduced bulk α-MoO_3 is less selective in propene oxidation, and formation of acrylic acid is hardly observed. Conversely, activated Mo_xO_y-VGCNF possessed a lower reducibility compared to bulk α-MoO_3 accompanied by complete re-oxidation to mainly Mo(VI) centers. It may be assumed that the characteristic shear-defects that form in bulk α-MoO_3 under reaction conditions and hinder complete re-oxidation at temperatures below 700 K do not form in the MoO_3 type molybdenum oxide species supported on VGCNF. Mo centers in the supported oxide may exhibit a local structure similar to that of α-MoO_3. However, the characteristic two- and three-dimensional layer structure of bulk α-MoO_3 may be absent in the supported catalyst. Hence, a different structure forms under reaction conditions, whose reduction and re-oxidation kinetic favor the selective oxidation of propene to acrylic acid.

Similar to supported hexagonal MoO_3 on SBA-15 [9] or heteropolyoxo molybdates [26], an improved selectivity correlated with a sufficiently rapid and complete re-oxidation to predominantly Mo(VI) centers. As stated above, the average Mo valence under reaction conditions is not a characteristic of a particular catalyst composition or local structure. It rather results from the characteristic reduction and re-oxidation kinetics of this structure under reaction conditions. Evidently, binary molybdenum oxides are capable of oxidizing propene to acrylic acid. Given favorable structural conditions we have shown that even a catalyst species possessing the local- and medium-range order structure of conventional α-MoO_3 may exhibit suitable redox kinetics and corresponding superior catalytic properties. Additional metal centers such as vanadium, niobium, or tungsten are not essential for this functionality, and structural complexity appears more important than chemical complexity.

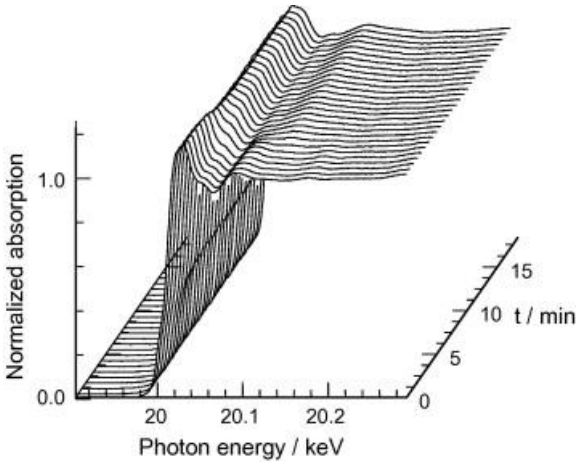

Fig. 15: Evolution of Mo K edge XANES spectra of activated Mo_xO_y-VGCNF measured during isothermal treatment in 3% propene in He at 673 K. After ~2.5 min oxygen was switched on and the sample treated in 3% propene/10% oxygen in He at 673 K.

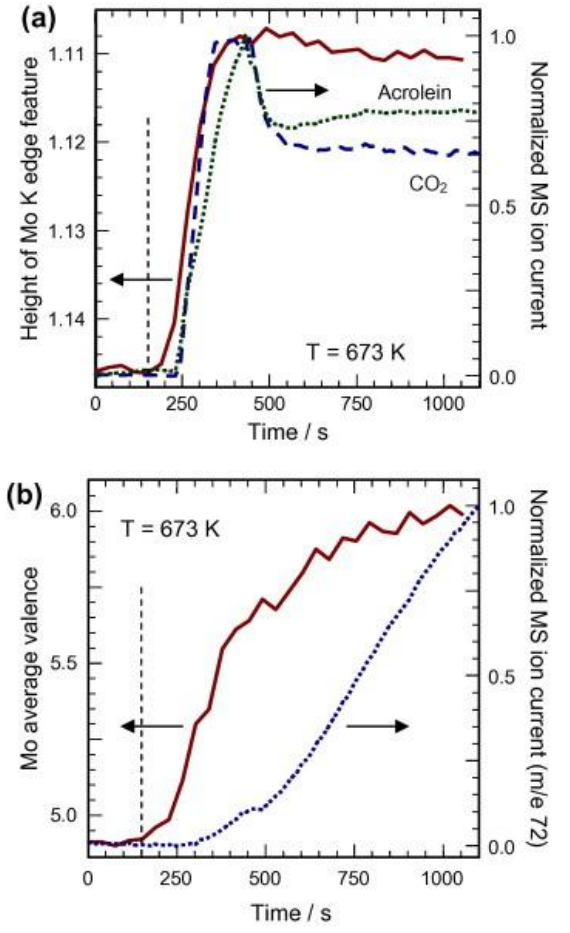

Fig. 16: (a) Evolution of normalized MS ion currents of CO_2 (m/e 44, dashed), acrolein (m/e 56, dotted), and Mo K edge peak height (solid) and (b) evolution of normalized MS ion current of acrylic acid (m/e 72, dotted) and Mo average Mo valence (solid) measured during isothermal treatment in 3% propene in He at 673 K. After 150 s oxygen was switched on (dashed line) and the sample treated in 3% propene/10% oxygen in He at 673 K.

4. Summary

In situ X-ray absorption spectroscopy under reaction conditions of selective propene oxidation was employed to elucidate the local structure of as-prepared and activated molybdenum oxide supported on carbon nanofibers. The local structure of as-prepared Mo_xO_y-VGCNF was very similar to that of hexagonal MoO_3. Compared to silica-based supports which may stabilize hex-MoO_3 at temperatures above 673 K, the presence of hex-MoO_3 on VGCNF results from moderate temperatures (<623 K) during catalyst preparation. During heat treatment in propene- and oxygen-containing atmosphere, as-prepared Mo_xO_y-VGCNF transforms into activated Mo_xO_y-VGCNF above 623 K. The local structure around the Mo centers in activated Mo_xO_y-VGCNF is similar to that of α-MoO_3. A slightly reduced amplitude is indicative of Mo oxide support interaction and small, layer-like MoO_3 species supported on VGCNF. Temperature and time-dependent XAS measurements showed a rapid transformation from hex-MoO_3 to α-MoO_3 supported on VGCNF under reaction conditions. Subsequently, the resulting activated Mo_xO_y-VGCNF catalyst exhibited a slowly increasing average oxidation state. The latter coincided with the formation of acrylic acid, which is hardly detectable during catalysis on regular, binary α-MoO_3. Moreover, activated Mo_xO_y-VGCNF is much more active in the selective oxidation of propene compared to α-MoO_3. Apparently, the particular local structure of "α-MoO_3"-like molybdenum oxide species supported on CNF permits a complete re-oxidation under reaction conditions in contrast to regular α-MoO_3. The correlation between catalytic selectivity and average oxidation state as a result of suitable reduction–oxidation kinetics corroborates the importance of structural complexity rather than chemical complexity.

Acknowledgements

The Hamburg Synchrotron Radiation Laboratory, HASYLAB, is acknowledged for providing beamtime for this work. The authors acknowledge financial support from the Deutsche Forschungsgemeinschaft, DFG (Cluster of Excellence "Unifying Concepts in Catalysis").

References

[1] B. Grzybowska-Swierkosz, *Topics in Catalysis* 2000, *11/12*, 23 - 42.
[2] R.K. Grasselli, *Catalysis Today* 1999, *49*, 141 – 153.
[3] J. Haber, E. Lalik, *Catalysis Today* 1997, *33*, 119 – 137.
[4] Mars, P., and van Krevelen, D.W., *Chem. Ing. Sci.* 3, 41 (1954).
[5] L.D. Krenzke, G.W. Keulks, *J. Catal.* 1980, *61*, 316 – 325.
[6] W. Ueda, Y. Moro-Oka, T. Ikawa, *J. Catal.* 1981, *70*, 409 – 417.
[7] T. Ressler, R.E. Jentoft, J. Wienold, T. Neisius, Journal of Catalysis, 210 (2002) 67 – 83.
[8] T. Ressler, J. Wienold, R.E. Jentoft, F. Girgsdies, Eur.J.Inorg.Chem., 2 (2003) 301-312.
[9] T. Ressler, A. Walter, Z.-D. Huang, W. Bensch, J. Catal. 254 (2008) 170–179.
[10] I.E. Wachs, Catal. Today 100 (2005) 79-94.
[11] K. Chen, S. Xie, A.T. Bell, E. Iglesia, J. Catal. 198 (2001) 232-242.
[12] S.H. Taylor, A.J.J. Pollard, Catal. Today 81 (2003) 179-188
[13] C. Hess, J. Catal. 248 (2007) 120-123.
[14] P. Serp, M. Corrias, P. Kalck, Appl. Catal. A 253 (2003) 337.
[15] A. Walter, R. Herbert, C. Hess, T. Ressler, Chemistry Central Journal, accepted.
[16] S.R. Bare, T. Ressler, Advances in Catalysis, 52 (2009) 339-465.
[17] J.-P. Tessonnier, D. Rosenthal, T.W. Hansen, C. Hess, M.E. Schuster, R. Blume, F. Girgsdies, N. Pfänder, O. Timpe, D.S. Su, R. Schlögl, *Carbon* 47 (2009) 1779-1798.
[18] J.-P. Tessonnier, T. W. Hansen, C. Hess, D. S. Su, R. Schlögl, in preparation.
[19] T. Ressler, R.E. Jentoft, J. Wienold, M.M. Günter, O. Timpe, J. Phys. Chem. B 104 (2000) 6360 - 6370.
[20] T. Ressler, J. Synch. Rad. 1998, 5, 118 – 122.
[21] J. J. Rehr, C. H. Booth, F. Bridges, S. I. Zabinsky, Phys. Rev. B 49 (1994) 12347 – 12350.
[22] [22] T. Ressler, S.L. Brock, J. Wong, S.L. Suib, J. Phys. Chem. B 103 (1999) 6407 – 6420.
[23] [http://www.ixasportal.net/ixas/images/ixas_mat/StandardsCriteria_July25_2000.pdf
[24] Numerical Recipes: The Art of Scientific Computing, Third Edition (2007), Cambridge University Press (www.nr.com).
[25] J. Wienold, R.E. Jentoft, T. Ressler, Eur.J.Inorg.Chem., 6 (2003) 1058-1071.
[26] T. Ressler, O. Timpe, Journal of Catalysis 247 (2007) 231-237.